Dynamics of the Pacific–North American Plate Boundary in the Western United States

Lucy M. Flesch,[1]* William E. Holt,[1] A. John Haines,[2] Bingming Shen-Tu[1]†

The vertically averaged deviatoric stress tensor field within the western United States was determined with topographic data, geoid data, recent global positioning system observations, and strain rate magnitudes and styles from Quaternary faults. Gravitational potential energy differences control the large fault-normal compression on the California coast. Deformation in the Basin and Range is driven, in part, by gravitational potential energy differences, but extension directions there are modified by plate interaction stresses. The California shear zone has relatively low vertically averaged viscosity of about 10^{21} pascal·seconds, whereas the Basin and Range has a higher vertically averaged viscosity of 10^{22} pascal·seconds.

Deformation within the western United States is distributed over hundreds of kilometers and is spatially complex. The Basin and Range is experiencing northwest-southeast extension, whereas the Pacific (PA)–North American (NA) Plate boundary is dominated by strike-slip earthquakes and compressional events near the coast of California. The Great Valley and Colorado Plateau (Fig. 1) remain relatively undeformed. Recent space-based geodetic measurements allowed accurate quantification of active strain rates throughout the western United States (*1*, *2*). Elsewhere, we have estimated a self-consistent velocity and strain rate field (*2*) determined with global positioning system (GPS) and very long baseline interferometry (VLBI) data (*1*) in the Basin and Range, Quaternary fault data for all onshore regions (*3*), and imposed NUVEL-1A (*4*) PA Plate motion (Fig. 1). The next step in continental dynamics involves understanding how the kinematics within this diffuse plate boundary zone relate to the forces driving deformation (*5*, *6*). Models of extensional driving forces in the Basin and Range can be grouped into three categories (*7*): plate boundary forces (*8*), basal tractions (*9*), and buoyancy forces (*10*, *11*). Many agree that any single one of these mechanisms is insufficient to drive all the deformation in the PA-NA boundary zone (*7*, *12*). To date, the individual contributions these forces make to the stress tensor field have not been quantified, and thus their relative role in influencing the deformation field has remained speculative.

Here, we quantify the individual stress field contributions from gravitational potential energy (GPE) variations within the lithosphere (buoyancy forces) and PA-NA Plate interaction (boundary forces), assuming the effects of basal tractions to be negligible (*13*). We estimated the GPE variations within the western United States using topographic (*14*) and geoid data (*15*). By treating the lithosphere as a viscous thin sheet of 100-km thickness (*16*) and making no assumptions about the rheology, we solved the force-balance equations (*17*) to determine the minimal vertically averaged deviatoric stress tensor field consistent with GPE variations (*18*). We determined deviatoric stresses over the entire western United States to avoid boundary effects but in the inversion described below only considered the gridded region in Fig. 2A, where strain rates determined there (*2*) help constrain stress boundary conditions. The stress tensor field due to GPE variations inferred from the topographic data (Fig. 2A) predicts absolute magnitudes of compressive stresses of ~10 MPa (100 bars) offshore of California and extensional stresses in the Basin and Range of 5 to 7.5 MPa. Although roughly E-W extension is predicted at the Wasatch Range, extensional stresses in the Great Basin are oriented at ~45° to the regional extension direction there. Therefore, GPE variations are insufficient to generate all Great Basin extension, and plate interaction must also be playing an important role.

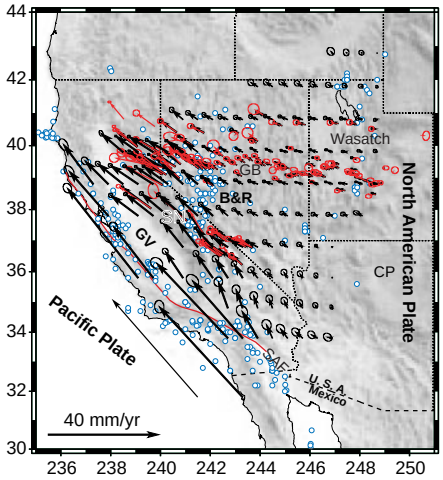

Fig. 1. A self-consistent, continuous velocity field solution (black arrows) (*2*) determined with GPS and VLBI data (red arrows) (*1*), Quaternary fault data (*3*), and imposed NUVEL-1A plate motion (*4*). Ellipses represent a 95% confidence limit. Blue dots represent seismicity recorded from 1850 to 1998. GV, Great Valley; B&R, Basin and Range; CP, Colorado Plateau; SAF, San Andreas fault; SN, Sierra Nevada; GB, Great Basin. Longitude and latitude are given in degrees east and north.

Assuming an isotropic relation between stress and strain rate (*19*), we determined stress field boundary conditions associated with plate interaction (*20*). These stress boundary conditions are found by matching the tensor styles of the total deviatoric stresses, combining the influences of both GPE variations and plate interactions, to the tensor styles of the observed strain rates. Strain rates in the 12 areas containing the San Andreas fault were not used in our calculations because the directions of principal strain rate there and inferred directions of principal stress are known to differ (*21*), implying an anisotropic relation between stress and strain rate (*22*). The deviatoric stress field due to plate interaction (Fig. 2B) predicts stresses consistent with strike-slip behavior with a tensional component throughout the region.

The vertically averaged total deviatoric stress field [linear sum of the stresses from GPE variations (Fig. 2A) and plate interactions (Fig. 2B) (*23*)] (Fig. 2C) predicts the direction and style of all major deformation within the western United States in accord with other stress estimates (*21*). In the model, compressional stresses on the San Andreas fault were rotated ~60° to the fault strike along the entire length of the fault. We showed that GPE variations (Fig. 2A) were responsible for orienting compressional deviatoric stresses at a high angle to the coastline (Fig. 2C) and for producing some of the convergent motion between the Sierra Nevada block and the Pacific Plate (Figs. 1 and 2D). We also showed that plate boundary interaction influences Great Basin extension, confirming that the history of extension in the Great Basin is linked with the history of PA-NA motion (*8*).

The total deviatoric stresses determined with GPE variations inferred from geoid data (Fig. 3) and those obtained with topographic data (Fig. 2C) differ most consistently offshore of California, where the stresses from geoid data were half as large. Elsewhere, the

[1]Department of Geoscience, State University of New York–Stony Brook, Stony Brook, NY 11794–2100, USA. [2]Bullard Laboratories, Cambridge University, Cambridge CB3 0EZ, UK.

*To whom correspondence should be addressed. E-mail: flesch@stillwater.ess.sunysb.edu

†Present address: Department of Geological Sciences, Indiana University, Bloomington, IN 47405, USA.

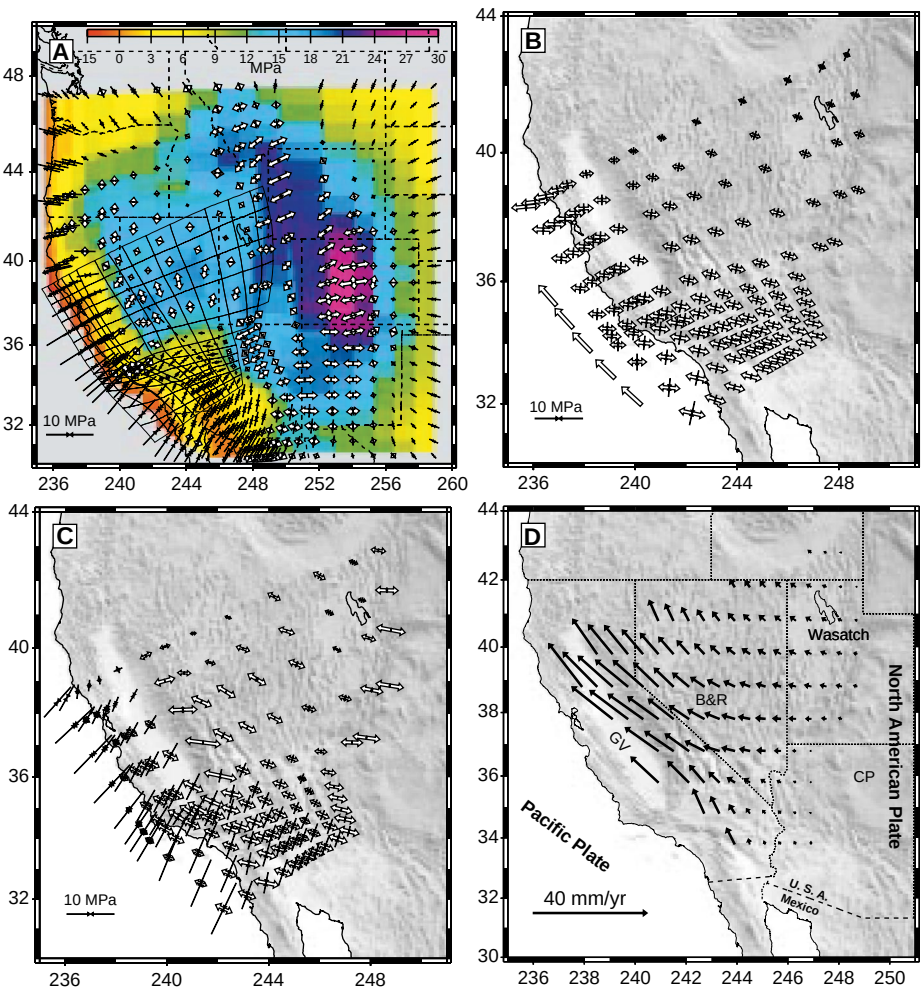

Fig. 2. (**A**) The minimal root mean squared deviatoric stress field determined from GPE variations, calculated assuming Airy compensation of topography. Different colors represent Δ GPE values $\bar{\sigma}_{zz}$ relative to a column of lithosphere at sea level. Tensional stress is shown as open white principal axes, and compressional stress is shown as black principal axes. (**B**) Stress field boundary conditions. The analog motion (open arrows) associated with these boundary conditions has a PA-NA pole that is ~10° west of the NUVEL-1A (*4*) PA-NA pole. (**C**) The total vertically averaged (over L = 100 km) deviatoric stress field, that is, the sum of stresses due to potential energy variations (A) and plate interaction (B). (**D**) The self-consistent flow field determined from strain rates calculated by scaling the total stress tensor field (C) by the inverse of viscosity (Fig. 4) for all areas east of the San Andreas fault (*32*).

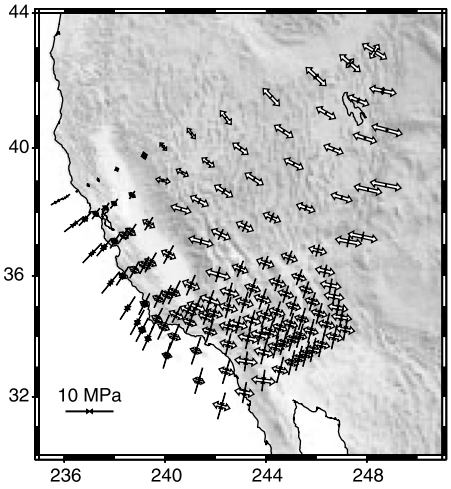

Fig. 3. The total deviatoric stress field determined from the sum of stresses due to GPE variations estimated with the filtered GEOID96 (*28*) and the corresponding best fit stress field boundary conditions associated with PA-NA Plate interaction.

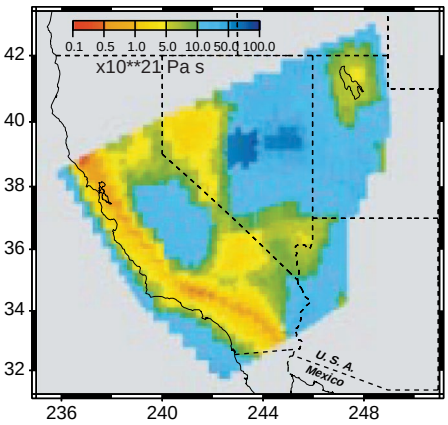

Fig. 4. The vertically averaged effective viscosity (over L = 100 km) for the western United States determined by dividing the magnitude of the total deviatoric stress (Fig. 2C) by the magnitude of the strain rate (*2*) for each grid area determined from the self-consistent kinematic model (Fig. 1).

two stress fields differ in magnitude by less than 50% and in direction by less than 5° almost everywhere.

Using the magnitude of the strain rate tensor derived for the western United States (*2*) and the magnitude of the total deviatoric stress tensor (Fig. 2C), we calculated vertically averaged effective viscosities (*19*) for the region (Fig. 4). Effective viscosity varies by three orders of magnitude over the western United States, with low values of ~5×10^{20} Pa·s along the San Andreas fault zone, 1 to 5×10^{21} Pa·s in the eastern California shear zone, and 2×10^{22} Pa·s in the Great Valley–Sierra Nevada block. The central Great Basin is relatively strong (3 to 7.5×10^{22} Pa·s) compared with the western margin of the Great Basin (2 to 8×10^{21} Pa·s). This contrast in effective viscosity is consistent with tomography results that suggest a depleted upper mantle in the central Great Basin (effectively strong) versus an upper mantle containing partial melt in the western Great Basin (effectively weak) (*24*). Relatively low values of effective viscosity in the lower crust and upper mantle (of order 10^{18} Pa·s) (*25*), when compared with our higher vertical averages, suggest that strong brittle upper crust is important in supporting the topography.

In all areas east of the San Andreas fault, we scaled our stress tensor by the inverse of the scalar effective viscosity to determine a combined kinematic and dynamic strain rate field (magnitudes the same as observed strain rates, but tensor style the same as stresses). From this strain rate field, a self-consistent horizontal velocity field (Fig. 2D) was determined with the method described by (*26*). The resulting flow field from the scaled stresses from GPE differences and plate interactions (Fig. 2D) resembles the kinematics inferred from recent GPS observations in the Basin and Range and Sierra Nevada (Fig. 1), confirming indirectly the good match we obtained between the tensor styles of the stress and the original strain rates.

References and Notes

1. R. A. Bennett, J. L. Davis, B. P. Wernicke, *Geology* **27**, 371 (1999); C. Ma and J. W. Ryan, NASA Space Geodesy Program—GSFC Data Analysis-1998, VLBI Geodetic Results 1979–1998 (NASA, Greenbelt, MD, 1998); W. Thatcher *et al.*, *Science* **283**, 1714 (1999).
2. B. Shen-Tu, W. E. Holt, A. J. Haines, *J. Geophys. Res.* **104**, 28927 (1999); B. Shen-Tu, W. E. Holt, A. J. Haines, *J. Geophys. Res.* **103**, 18087 (1998).
3. C. W. Jennings, Fault Activity Map of California and

Adjacent Areas (California Department of Conservation, Division of Mines and Geology, Sacramento, CA, 1994); M. D. Petersen and S. G. Wesnousky, *Bull. Seismol. Soc. Am.* **84**, 1608 (1994).
4. C. DeMets, R. G. Gordon, D. F. Argus, S. Stein, *Geophys. Res. Lett.* **21**, 2191 (1994).
5. P. England and P. Molnar, *Science* **278**, 647 (1997).
6. L. M. Flesch, A. J. Haines, W. E. Holt, in preparation.
7. L. J. Sonder and C. H. Jones, *Annu. Rev. Earth Planet. Sci.* **27**, 417 (1999); B. Wernicke, *The Cordilleran Orogen; Conterminous U.S.*, vol. G-3 of *The Geology of North America*, B. C. Burchfiel, P. W. Lipman, M. L. Zoback, Eds. (Geological Society of America, Boulder, CO, 1992), pp. 553–581.
8. T. Atwater, *Geol. Soc. Am. Bull.* **81**, 3513 (1970); J. Stock and P. Molnar, *Tectonics* **7**, 1339 (1988); R. G. Bohannon and T. Parsons, *Geol. Soc. Am. Bull.* **107**, 937 (1995).
9. D. P. McKenzie, *Geophys. J. R. Astron. Soc.* **18**, 1 (1969); A. Tovish, G. Schubert, B. P. Luyendyk, *J. Geophys. Res.* **83**, 5892 (1978).
10. L. Fleitout and C. Froidevaux, *Tectonics* **1**, 21 (1982).
11. C. H. Jones, L. J. Sonder, J. R. Unruh, *Nature* **381**, 37 (1996).
12. S. Wdowinski and R. O'Connell, *J. Geophys. Res.* **96**, 12245 (1991); M. Liu and Y. Shen, *Tectonics* **17**, 311 (1998).
13. Basal tractions have a significant effect on the total stress field only if horizontal path integrals of basal tractions are of the same order of magnitude as the vertically averaged horizontal stress times the thickness of the lithosphere (10 MPa × 100 km).
14. We estimated the vertically averaged vertical stress, expressed as $\bar{\sigma}_{zz} = 1/L \int_{-h}^{L} \int_{-h}^{z} g\rho dz dz$, where ρ is the density, h is the surface elevation, L is an average thickness of the lithosphere, which was chosen to be 100 km here and was applied to the whole region as the scaling factor 1/L, and g is gravity (*5*, *11*). Assuming local (Airy) isostatic compensation, $\bar{\sigma}_{zz}$ was calculated assuming crustal and mantle densities of 2750 kg/m^3 and 3300 kg/m^3, respectively. We also used the geoid anomaly to infer GPE variations (*27*). The geoid anomaly incorporates effects of lateral density variations in both the crust and mantle and is not dependent on an assumed mechanism of compensation of topography.
15. We used the GEOID96 model (*28*) and removed terms below degree and order 7 with a cosine taper to degree and order 11 (*11*, *29*), because of a signal in the geoid from heterogeneities deep within the mantle (*30*). Following the method of (*27*), we calculated GPE estimates for the western United States using a column at sea level for reference.
16. P. England and D. P. McKenzie, *Geophys. J. R. Astron. Soc.* **70**, 295 (1982).
17. The equation of steady state motion is $\partial\sigma_{ij}/\partial x_j + \rho g \hat{z}_i = 0$, where ρ is density, g is gravity, $\hat{z}_i$ is the unit vector in the z direction, σ_{ij} is total stress, and x_j is the jth coordinate direction. We make two assumptions consistent with viscous fluid methodology: (i) that deviatoric stress can be averaged in the same fashion to the depth L (100 km) as σ_{zz} (*14*) and (ii) that tractions at the base of the lithosphere are negligible. Making these two assumptions, the horizontal-component force-balance equations condense to $\partial/\partial x_\beta(\bar{\tau}_{\alpha\beta} + \delta_{\alpha\beta}\bar{\tau}_{\gamma\gamma}) = -(\partial\bar{\sigma}_{zz}/\partial x_\alpha)$, where $\bar{\tau}_{\gamma\gamma} = \bar{\tau}_{xx} + \bar{\tau}_{yy} = -\bar{\tau}_{zz}$, x_α is the α coordinate direction, $\bar{\tau}_{\alpha\beta}$ is the deviatoric stress tensor, $\delta_{\alpha\beta}$ is the Krunecker delta function, and $\bar{\sigma}_{zz}$ is the vertically averaged vertical stress (potential energy), which is used as input (*6*).
18. We used the variational principle (*31*) to minimize the functional $I = \int_S [\bar{\tau}_{\alpha\beta}\bar{\tau}_{\alpha\beta} + (\bar{\tau}_{\gamma\gamma})^2] dS + \int_S 2\lambda_\alpha [(\partial/\partial x_\beta)(\bar{\tau}_{\alpha\beta} + \delta_{\alpha\beta}\bar{\tau}_{\gamma\gamma}) + (\partial\bar{\sigma}_{zz}/\partial x_\alpha)] dS$ with respect to $\hat{\tau}_{\alpha\beta}$, where S is the area of Earth's surface being considered and λ_α is the Lagrange multiplier for the differential equation constraint (*17*), which yields the requirements that $\bar{\tau}_{\alpha\beta} = {}^1/_2[(\partial\lambda_\alpha/\partial x_\beta) + (\partial\lambda_\beta/\partial x_\alpha)]$ and the vector $\lambda_\alpha = 0$ everywhere on ∂S. Again using the variational principle, minimization of the functional
$$J = \int_s \left[2\left(\bar{\tau}_{xx} + \frac{1}{3}\bar{\sigma}_{zz}\right)^2 + 2\left(\bar{\tau}_{xx} + \frac{1}{3}\bar{\sigma}_{zz}\right) \times \left(\bar{\tau}_{yy} + \frac{1}{3}\bar{\sigma}_{zz}\right) + 2\left(\bar{\tau}_{yy} + \frac{1}{3}\bar{\sigma}_{zz}\right)^2 + 2\,\bar{\tau}_{xy}^2 \right] dS$$
with respect to λ_α provides a self-consistent solution to the force-balance equations (*17*). These expressions were for the flat-Earth approximation, but we were actually using the corresponding expressions for the spherical Earth (*6*), which have the same structure but less simple forms.
19. In isotropic media, stress, $\bar{\tau}_{\alpha\beta}$, and strain rate, $\dot{\varepsilon}_{\alpha\beta}$, are related by $\bar{\tau}_{\alpha\beta} = \bar{\eta}\dot{\varepsilon}_{\alpha\beta}$, where $\bar{\eta}$ is the effective viscosity for a power law fluid rheology (*16*).
20. We solved for three stress field basis functions, defined by three separate sets of Lagrange multiplier values, $\Lambda_i = (\lambda_\alpha, \lambda_\beta)$, assigned to the PA Plate boundary and applied in the functionals *I* and *J* (*18*). Minimization of functional *J* (*18*) again satisfies force-balance equations (*17*) with $\bar{\sigma}_{zz}$ now set to zero in the functionals. The assigned values for Λ_i define the specific stress field boundary conditions for the three stress field basis functions and were the three most spatially uniform cases $\Lambda_i = \omega_i \times r$, where r marks the radial position vector along the PA Plate boundary and ω_i are three orthogonal rotation vectors (0°N, 0°E, 1), (0°N, 90°E, 1), and (90°N, 0°E, 1). A linear combination of the three stress field basis functions (Fig. 2B), added to the deviatoric stresses associated with GPE variations (Fig. 2A), defined the total stress field (Fig. 2C). The coefficients of the three basis functions in this linear combination are found by iterative least squares inversion for the best fit between the tensor styles of the resulting total stress field and the styles inferred from stress indicators (*2*) [that is, the styles of the strain rates inferred from GPS and VLBI data (*1*), Quaternary fault data (*3*), and imposed NUVEL-1A plate motion (*4*)] (*6*).
21. M. D. Zoback *et al.*, *Science* **238**, 1105 (1987); V. S. Mount and J. Suppe, *Geology* **15**, 1143 (1987); A. H. Lachenbruch and J. H. Sass, *J. Geophys. Res.* **97**, 4995 (1992); M. L. Zoback, *J. Geophys. Res.* **94**, 7105 (1989); M. L. Zoback, *J. Geophys. Res.* **97**, 11703 (1992).
22. L. E. Gilbert, C. H. Scholz, J. Beavan, *J. Geophys. Res.* **99**, 23975 (1994).
23. Because the force-balance equations in (*17*) are linear in stress, any number of solutions can be superimposed. This is true even for power law rheology. Stresses resulting from individual tectonic sources (boundary forces) and internal buoyancy effects (body forces) can be added linearly. What does not add linearly with a power law rheology is strain rate.
24. E. D. Humphreys and K. G. Duker, *J. Geophys. Res.* **99**, 9635 (1994); M. Liu and Y. Shen, *Geology* **26**, 299 (1998).
25. B. G. Bills, D. R. Currey, G. A. Marshall, *J. Geophys. Res.* **99**, 22059 (1994); B. G. Bills, K. D. Adams, S. G. Wesnousky, *Eos* **76**, 608 (1995); J. Deng, M. Gurnis, H. Kanamori, E. Hauksson, *Science* **282**, 1689 (1998); F. F. Pollitz, G. Peltzer, R. Burgmann, *Eos* **79**, F601 (1998).
26. A. J. Haines and W. E. Holt, *J. Geophys. Res.* **98**, 12057 (1993).
27. D. D. Coblentz, R. M. Richardson, M. Sandiford, *Tectonics* **13**, 929 (1994).
28. D. A. Smith and D. G. Milbert, *J. Geodesy* **73**, 219 (1999).
29. A. F. Sheehan and S. C. Solomon, *J. Geophys. Res.* **96**, 19981 (1991).
30. B. H. Hager, R. W. Clayton, M. A. Richards, R. P. Comer, A. M. Dziewonski, *Nature* **331**, 541 (1985).
31. P. M. Morse and H. Feshbach, in *Methods of Theoretical Physics* (McGraw-Hill, New York, 1953), pp. 275–347.
32. The San Andreas fault may be weak in the direction of slip (*22*) and therefore rheologically anisotropic. When we assigned the strain rates from the kinematic solution (*2*) to the 12 areas containing the San Andreas fault, we obtained the full PA-NA Plate motion.
33. We thank W. Thatcher and his group for allowing us use of their GPS data before publication, C. Jones for sharing the geoid filtering code, and two anonymous reviewers. Maps were prepared with GMT version 3.0 by P. Wessel and W.F. Smith. This work was supported by an NSF career grant to W.E.H. (EAR- 962 8872) and U.S. Geological Survey grant 99HQGR0010. A.J.H.'s contribution has been supported by the Marsden Fund administered by the Royal Society of New Zealand.

22 September 1999; accepted 6 December 1999

High-Speed Electrically Actuated Elastomers with Strain Greater Than 100%

Ron Pelrine,* Roy Kornbluh, Qibing Pei, Jose Joseph

Electrical actuators were made from films of dielectric elastomers (such as silicones) coated on both sides with compliant electrode material. When voltage was applied, the resulting electrostatic forces compressed the film in thickness and expanded it in area, producing strains up to 30 to 40%. It is now shown that prestraining the film further improves the performance of these devices. Actuated strains up to 117% were demonstrated with silicone elastomers, and up to 215% with acrylic elastomers using biaxially and uniaxially prestrained films. The strain, pressure, and response time of silicone exceeded those of natural muscle; specific energy densities greatly exceeded those of other field-actuated materials. Because the actuation mechanism is faster than in other high-strain electroactive polymers, this technology may be suitable for diverse applications.

New high-performance actuator materials capable of converting electrical energy to mechanical energy are needed for a wide range of demanding applications, such as mini- and microrobots, micro air vehicles, disk drives, flat-panel loudspeakers, and prosthetic devices. Many types of candidate materials are under investigation, including single-crystal piezoelectric ceramics (*1*) and carbon nanotubes (*2*). Electroactive polymers are of particular interest because of the low cost of materials and the

SRI International, 333 Ravenswood Avenue, Menlo Park, CA 94025, USA.

*To whom correspondence should be addressed. E-mail: pelrine@erg.sri.com